Renewable Energy 143 (2019) 313–327

Contents lists available at ScienceDirect

Renewable Energy

journal homepage: www.elsevier.com/locate/renene

Dynamic modeling and verification of a proton exchange membrane fuel cell-battery hybrid system to power servers in data centers

Sanggyu Kang [a, *], Li Zhao [b], Jacob Brouwer [b]

[a] Korea Institute of Machinery and Materials, Daejeon 305-343, Republic of Korea
[b] National Fuel Cell Research Center, University of California, Irvine, CA, 92697, USA

ARTICLE INFO

Article history:
Received 28 February 2019
Received in revised form
11 April 2019
Accepted 27 April 2019
Available online 10 May 2019

Keywords:
Proton exchange membrane fuel cell (PEMFC)-Battery hybrid system
Dynamic modeling
Validation
Control strategy
Data centers

ABSTRACT

Dynamic performance of a 10-kW proton exchange membrane fuel cell (PEMFC)–battery hybrid system to power servers in data centers has been experimentally evaluated in our previous work [1]. The present work is a numerical study based on the previous work to identify the dynamic characteristics and present basic insights for the system control strategy during transients. The hybrid system dynamic model has been developed using the MATLAB–Simulink®, which consists of a one-dimensional, two-phase dynamic model of the PEMFC, lumped dynamic model of an air blower and a battery. The system model is verified by comparing the dynamic behavior of the power generated by the PEMFC and battery with the experimental data at the step change of the system demand power between 0 and 1.5, 3.0, 4.5, 6.0, 7.5, and 9.0 kW. During the step load increases, the system instantly obtained the total amount of external load power from the battery within 0.1 s in every case and gradually decreased until approximately 4 s or 6 s as the power generated by the fuel cell is gradually increased. The dynamic response of the system model is compared with the experimental data at various load profiles of three, six, and nine servers.

1. Introduction

Fuel cells have been regarded as a promising candidate of alternate power generation for automotive applications and stationary power plants due to their fast response, low emission, high power density, and high efficiency [2,3]. As the energy consumption of data centers has increased up to 70 billion kWh per year in 2014, fuel cells have recently received particular attention as a power supply for the data centers [4]. Thus, a few attempts have been made to utilize fuel cells in power servers of data centers. For example, eBay Inc. installed a 6-MW fuel cell, a product of Bloom Energy®, in their Utah data centers with a parallel grid configuration [5]. Given that most data centers currently use the utility grid to power their servers, eBay uses fuel cells as a backup power to increase its reliability and safety of the grid during transients. The National Fuel Cell Research Center (NFCRC) proposed a fuel cell system, which is inches from servers, to power servers at the rack level [1]. With the distributed fuel cell (DFC) configuration, many equipment of power distribution units, high-voltage transformers, switchgears, and AD–DC power supplies from data centers can be removed [1]. The NFCRC demonstrated and evaluated a DFC architecture that places the 10-kW proton exchange membrane fuel cell (PEMFC)–battery hybrid system at the rack level inches from the servers. Because servers in data centers require large changes in load power in a short time, the NFCRC experimentally estimated the dynamic performance and reliability of the PEMFC–battery hybrid system under various load changes [1].

To utilize the PEMFC–battery hybrid system as a power source for servers in data centers, the load-following capability of the PEMFC–battery hybrid system is paramount. Several researchers have investigated the dynamic performance of a PEMFC stack. Tang et al. captured the dynamic behavior of a PEMFC stack at various load changes by using the commercial PEMFC system of the Nexa module [6]. The researchers experimentally analyzed the effects of operating conditions such as temperature, air flow rates, and current on the dynamic performance of a PEMFC. Loo et al. captured the dynamic response of the PEMFC with the presence of cathode flooding by using a one-dimensional, two-phase model [7]. Cho et al. captured the effect of a gas diffusion layer (GDL) degradation on the dynamic behavior of a PEMFC [8]. The degradation of GDL results in a lower voltage response and flooding because of the non-

* Corresponding author.
E-mail address: kyu2613@kimm.re.kr (S. Kang).

https://doi.org/10.1016/j.renene.2019.04.150
0960-1481/

Nomenclature

a	Water activity [−]
A	Surface area [m^2]
C	Specific heat capacity [$kJkg^{-1}K^{-1}$]
$\overrightarrow{C}$	Molar concentration [$kmolm^{-3}$]
D	Diameter [m]
D_w	Water diffusion coefficient through electrolyte [m^2s^{-1}]
D_λ	Water diffusivity in Nafion [m^2s^{-1}]
$\overrightarrow{D}$	Species diffusion coefficient through GDL [$m^2\ s^{-1}$]
F	Faraday's constant [$Cmol^{-1}$]
f	Friction factor [−]
ΔG	Gibbs energy [$kJkmol^{-1}$]
$\overrightarrow{g}$	Gravitational acceleration [ms^{-2}]
h	Convection coefficient [$kWK^{-1}m^{-2}$], or Enthalpy [$kJkmol^{-1}$]
hd	Head loss [m]
ΔH	Formation enthalpy [$kJkmol^{-1}$]
i	Current [A]
J	Inertia [kgm^2]
$J(s)$	Leverette function [−]
$\overrightarrow{l}$	Liquid water flux [$kmols^{-1}$]
L	Length [m]
N	Number of fuel cell [−]
$\dot{N}$	Molar flow rate [$kmols^{-1}$]
n	Electron number [−]
n_d	Electro-osmotic drag coefficient [−]
p	Pressure [kPa]
$\dot{Q}$	Heat transfer rate [kW]
R	Universal gas constant [8.3145 $kJkmol^{-1}K^{-1}$], or battery resistance [ohm], or reaction rates [$kmols^{-1}$]
s	Liquid water saturation factor [−]
$Sher$	Sherwood number [−]
SOC	State of charge [−]
T	Temperature [K]
t	Time [s]
V	Voltage [V], or velocity [ms^{-1}]
v	Volume [m3]
$\overrightarrow{X}$	Species mole fraction [−]

Greek letters

α	Activation overpotential tuning coefficient [−]
β	Ohmic overpotential tuning coefficient [−]
γ	Activation energy [kJ/kg]
ε	GDL Mean porosity [−]
I	Diffusion flux through GDL [$kmols^{-1}$]
Ω_{H_2O}	Water diffusion flux through electrolyte [$kmols^{-1}$]
Ξ_{H_2O}	Electro-osmotic flux [$kmols^{-1}$]
η	Efficiency [−]
ω	Angular velocity [rpm]
λ	Stoichiometric ratio [−], or membrane water content [−]
K	Permeability [m^2]
τ	Surface tension [Nm^{-1}], or torque [Nm]
ρ	Density [kgm^{-3}]
θ	Contact angle [°]

Subscripts

actual	Actual
air	Air
b	Battery
blower	Air blower
c	Capillary
eff	Effective
H	Hydraulic
H_2	Hydrogen
ht	Heat transfer
H_2O	Water
in	inlet
initial	Initial
l	Long time, or liquid
lat	Latent
mea	Membrane
motor	Electric motor
o	Standard condition
O_2	Oxygen
out	Outlet
pore	Pore
ref	Reference condition
s	Solid, or short time
sat	Water saturation
target	Target

uniform hydrophobicity in the GDL. The influence of the flow-field design, cell temperature, and charge double layer on the dynamic behavior of PEMFC has been investigated via the numerical model of Tiss et al. [9]. The researchers concluded that the dominant factor to determine the PEMFC dynamic performance is the load resistance and functioning temperature. Gomez et al. investigated the influences of operating parameters on the dynamic response of a dead-end PEMFC stack [10]. The researchers insisted that the most dominant factor that causes the performance degradation is the nitrogen crossover from the cathode and the accumulation of liquid water at the anode. The PEMFC transient response of various operating parameters has been investigated by Kim et al. [11]. The optimal value for the air excess and air stoichiometry ratios were determined to minimize the undershoot and voltage fluctuation during transients. However, these studies are limited to focus on the dynamic response of the PEMFC stack.

Several investigations have been performed regarding the PEMFC–battery hybrid system. Tang et al. manufactured a hybrid system that integrates a lead-acid battery pack and a 2-kW PEMFC stack for lightweight cruising vehicles [12]. The researchers analyzed the dynamic behavior of the PEMFC stack and battery with road test experiments. Barelli et al. developed a dynamic modeling of a PEMFC–battery hybrid system for bus applications [13]. The researchers determined the fuel cell and battery output power by simulating the model under an actual driving load profile during a half-day operation. An energy management system (EMS) for a fuel cell hybrid vehicle (FC-HEV) has been presented by Ettihir et al. [14]. To verify the proposed adaptive EMS that is employed in two PEMFC systems with different degrees of degradation, an energy management strategy based on differential power processing compensation and fuzzy logic hysteresis state machine was proposed by Peng et al. [15] for the PEMFC hybrid tramway system. The overall system efficiency could be enhanced by 7% by using their proposed control strategy. Hong et al. developed an energy management control for a scaled-down locomotive system composed of a PEMFC and battery pack [16]. The hydrogen consumption was

reduced by 0.86 g and the system efficiency was improved by 2% by employing their proposed control strategy. Li et al. presented an equivalent consumption minimum strategy (ECMS) based on sequential quadratic programming for the FC-HEV composed of a fuel cell, battery, and supercapacitor [17]. The researchers experimentally verified that the proposed ECMS could decrease the hydrogen consumption by 2.16%. In addition, Fathabadi et al. proposed a novel fuel cell–battery hybrid system composed of a 90-kW PEMFC stack and a 19.2-kWh Li-ion battery for FC-HEVs [18]. The researchers established a system prototype and performed the experiments to confirm the feasibility of their proposed system. Most studies on the PEMFC–battery hybrid system has focused on automotive applications. Only a few have focused on the PEMFC–battery hybrid system for powering servers in data centers.

The present study is an extended work from the experimental work previously achieved in the NFCRC [1]. Because the previous study is only the experimental work using the commercialized product of PEMFC and battery, the PEMFC-battery hybrid system has been operated at the limited operating conditions. To ensure safe and efficient operation and to develop control strategies for the PEMFC-battery hybrid system, it is crucial to understand both the steady and dynamic performance characteristics of the hybrid system. This study is the first step to develop the optimal system designs and operating strategies for the PEMFC-battery hybrid system for powering servers in data centers. The present work aims to develop a dynamic model of the PEMFC–battery hybrid system to power servers in data centers by using the MATLAB–Simulink® software. The PEMFC–battery hybrid system model consists of a one-dimensional, two-phase dynamic model of the PEMFC stack; zero-dimensional dynamic model of an air blower; lumped dynamic battery model; and system power controller. The PEMFC is discretized into 11 and 15 control volumes in the flow-perpendicular direction to resolve mass and energy conservation, respectively. The lumped dynamic model of an air blower model was developed by considering the inertia of a blower and motor to capture the dynamic response of the blower. The lumped dynamic battery model is developed using the resistance and capacitance (R–C) ladder model. The system power controller is developed on the basis of a proportional integration (PI) controller to determine the input current for the PEMFC stack with various external load changes. The dynamic model of the PEMFC stack was validated at the steady state and during transients by comparing the current–voltage polarization curve and the dynamic behavior of the current and voltage with the experiments, respectively. Moreover, the PEMFC–battery hybrid system model was verified during transients by comparing the dynamic behavior of the respective power generated by the PEMFC stack and the battery with the experimental data. The dynamic performance of the system model was compared with the experimental data at the demand load power profile of three, six, and nine servers. The variations in the PEMFC characteristics of water flux and irreversible voltage losses have been investigated. Meanwhile, the variations in the battery state of charge (SOC) and air blower power consumption were identified. The model is beneficial in investigating the dynamic characteristics of the PEMFC–battery hybrid system during transients. This work also can contribute to the development of the optimal control strategy for the PEMFC–battery hybrid system to achieve stability for powering servers in data center under various load changes.

2. Model description

2.1. PEMFC–battery hybrid system

The reference for the PEMFC–battery hybrid system model developed in the current work is the Hydrogenics HYPM^{TM}R 10 fuel cell rack system, which is composed of HYPM™ XR 12 PEMFC and APC Smart-UPS™ VT™ 15 kVA UPS based on lead-acid batteries [1]. The 48-V DC output current from the PEMFC stack was converted to a 192-V DC by using a DC/DC converter because the UPS system can only use 192-V DC as the input [1]. Subsequently, the UPS system converted the DC power into the AC power via the DC/AC inverter to supply the required power for the connected server/load. The HYPM™ XR 12 PEMFC system comprises a PEMFC stack (rated at 12 kW, 48-V DC), a DC/DC converter (±192-V DC), the balance of plant (BOP), and a system controller. The fuel and air flow rates were controlled by the respective valves and blowers via the system controller. Both fuel and air were not humidified and heated before entering the stack. For safety purposes, both the anode and cathode exhaust gases from the PEMFC stack were continuously ventilated by the blower, which was powered by the PEMFC system. Although the system was not connected to the external load, the PEMFC system should supply the power to operate the ventilation blower. The heat generated from the PEMFC stack was rejected by the coolant water. Subsequently, the coolant water was cooled down via by tap water flowing through the heat exchanger. To determine the dynamic response of the in-rack PEMFC–battery hybrid system, the system dynamic model comprising a PEMFC stack, air blower, battery, and system power controller was established. Each component was developed and integrated to a system model to investigate the dynamic characteristics of the PEMFC–battery hybrid system. Fig. 1 shows the simulation flow chart of the PEMFC–battery hybrid system. When load power is required in the system, the system power controller determines the demand current to the PEMFC stack. The net power of the PEMFC system is obtained by subtracting the power consumed by the air blower, ventilation blower, and auxiliary BOP from the power generated from the PEMFC stack. In battery discharging mode, the difference between the demand and output current of the PEMFC system is supplied from the battery. Meanwhile, the battery recovers the SOC by obtaining the current from the PEMFC system in the charging mode.

2.2. PEMFC

In the current work, the PEMFC–battery hybrid system model was developed for the system design and control optimization. A multidimensional PEMFC model can capture the detailed phenomena occurring in the PEMFC. However, it is not suitable for the system simulation because of the high computational time. Hence, a two-phase, one-dimensional dynamic model of the PEMFC stack from our previous work was used [19]. The specifications of the PEMFC stack used in the current work is presented in Table 1. In resolving the species conservation, the PEMFC model is discretized into 11 control volumes of three types, namely, gas channel, GDL, and electrolyte in the cross-sectional direction, as shown in Fig. 2-(a). Meanwhile, the PEMFC model is discretized into 15 control volumes of six types, namely, solid plate, gas channel, GDL, electrolyte, cooling channel, and cooling plate flowing in perpendicular direction to resolve the energy balance, as shown in Fig. 2-(b). The model resolves the two-phase liquid water transport through the GDL to determine the liquid water effect on the PEMFC performance.

2.2.1. Species conservation

In the anode and cathode channel, dynamic species conservation equation has been resolved to determine the outlet species mole flow rate:

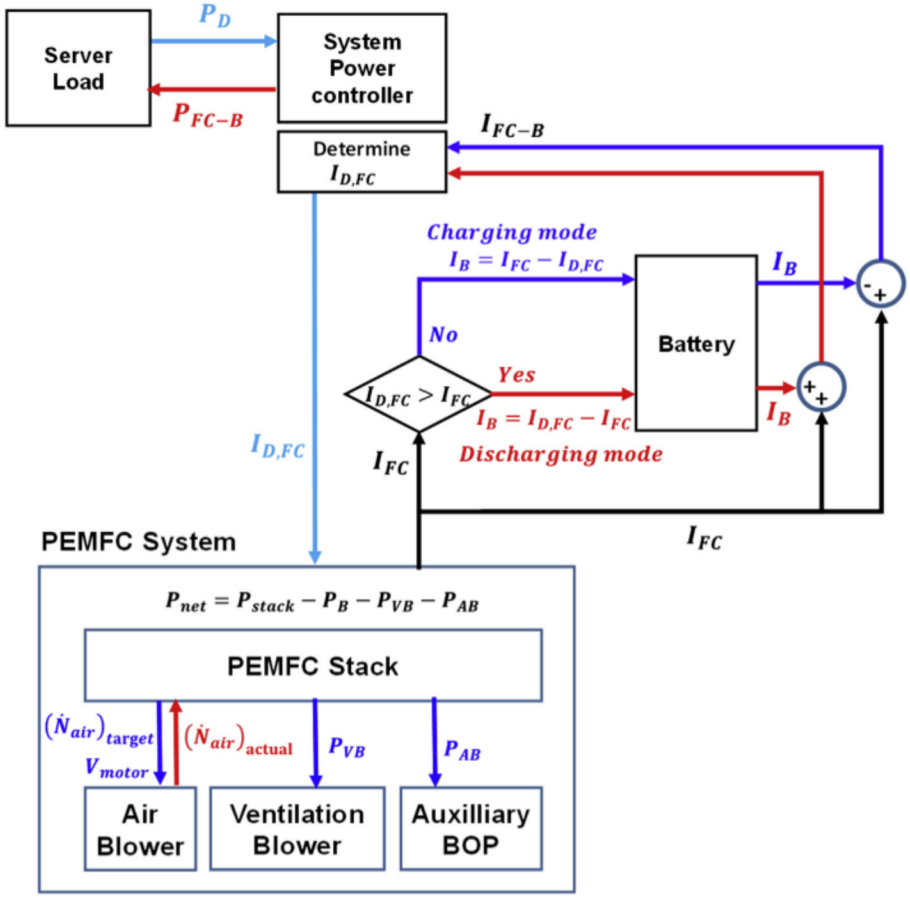

Fig. 1. Simulation flow chart for the PEMFC–battery hybrid system.

$$\frac{d\left(N\vec{X}\right)}{dt} = \dot{N}_{in}\vec{X}_{in} - \dot{N}_{out}\vec{X}_{out} + \sum I \tag{1}$$

where I is the mass transfer rate from the GDL via diffusion. The species mole fraction at the GDL is calculated:

$$\frac{d\vec{N}}{dt} = -\sum I + \sum \Omega_{H_2O} + \sum \Xi_{H_2O} + \vec{R} - \vec{l} \tag{2}$$

where $\vec{R}$, Ω_{H_2O}, Ξ_{H_2O}, and $\vec{l}$ are the electrochemical reaction rates, back diffusion, electro-osmotic drag, and liquid water flux through GDL, respectively.

Table 1
The PEMFC specifications.

Parameters	Units	Values
Maximum stack power	kW	10
Cell number	–	60
Cell active area	m^2	0.012
Height of anode channel (z)	m	0.001
Height of cathode channel (z)	m	0.001
Height of cooling channel (z)	m	0.001
GDL thickness (z)	m	0.0002
Electrolyte thickness (z)	m	30.48×10^{-6}
Thickness of separator plates (z)	m	0.002
GDL mean porosity	–	0.5

2.2.2. Energy conservation

Dynamic energy conservation equation determined the solid plate temperature:

$$\frac{dT}{dt} = \frac{\sum \dot{Q}_{ht}}{\rho v C} \tag{3}$$

where $\dot{Q}_{ht}$ is heat transfer rate to the control volume. The gas and

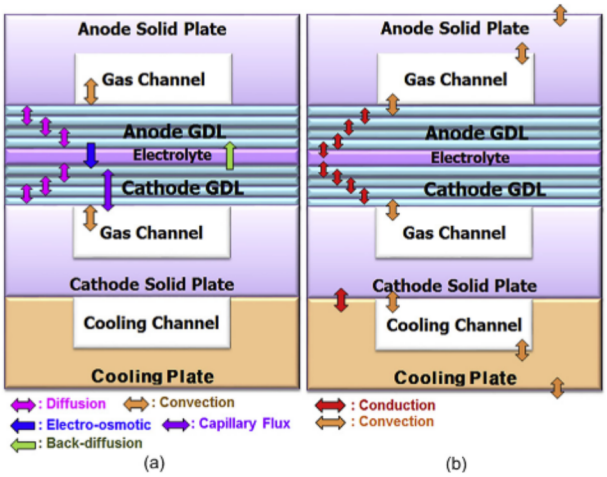

Fig. 2. Schematic of the PEMFC discretization for (a) mass balance and (b) energy balance (not drawn to scale).

the coolant channel temperatures are calculated:

$$\frac{dT}{dt} = \frac{\sum \dot{N}_{in} h_{in} - \sum \dot{N}_{out} h_{out} + \sum \dot{Q}_{ht} + \sum \dot{Q}_{lat}}{NC_V} \tag{4}$$

where $\dot{N}_{in} h_{in}$ and $\dot{N}_{out} h_{out}$ is the enthalpy flux into or out of the control volume, respectively. $\dot{Q}_{lat}$ is the liquid water latent heat. The temperature of both the GDL and the electrolyte are calculated by the dynamic energy conservation:

$$\frac{dT}{dt} = \frac{\sum \dot{Q}_{in} + \sum \dot{Q}_{lat} + \dot{N}_{in} h_{in} - \dot{N}_{out} h_{out} + \Delta H \cdot \frac{i}{nF} - \frac{V \cdot i}{1000}}{\left(\sum (\rho v C)_s + \sum (NC)_l\right)} \tag{5}$$

where, i, V, and ΔH are the current, and the voltage, and the enthalpy of water formation, respectively. $(\rho v C)_s$ and $(NC)_l$ are the thermal mass of solid and liquid water, respectively.

2.2.3. Heat transfer

As shown in Fig. 2, heat is produced in the electrolyte, and which is transferred to the GDL by both conduction and convection. The conductive heat transfer occurs between the solid plate and the GDL. The convective heat transfer occurs between the GDL and the gas in the channel.

2.2.4. Species diffusion

In this model, diffusion and the convection are considered the dominant species transport through the GDL channel and channel, respectively. The convective transport coefficient in the channel is calculated:

$$\vec{H} = \frac{Sher \cdot \vec{D}}{D_H} \tag{6}$$

where D_H, $\vec{D}$, and $Sher$ are the hydraulic diameter, the diffusion coefficient, and the Sherwood number, respectively. The diffusion coefficients has been modified to consider the effects of porosity and tortuosity in the GDL by the Bruggeman correlation:

$$\vec{D} = \vec{D}_o \left(\frac{T}{T_o}\right)^{3/2} \left(\frac{P_o}{P}\right) \tag{7}$$

$$\vec{D}_{eff} = \varepsilon (1 - s)^{1.5} \cdot \vec{D} \tag{8}$$

where ε, s, and $\vec{D}_{eff}$ are the GDL porosity, liquid water saturation factor, and the effective species diffusion coefficient, respectively.

2.2.5. Water transport

The water transfer rate due to the electro-osmotic drag is proportional to the current density:

$$\Xi_{H_2O} = n_d \cdot \frac{i}{A \cdot F} \tag{9}$$

where n_d is the osmotic drag coefficient through the Nafion® membrane, which is calculated by the membrane water content [20]:

$$n_d = \begin{Bmatrix} 1.0 & for\ \ \lambda \le 14 \\ \frac{1.5}{8}(\lambda - 14) + 1.0 & otherwise \end{Bmatrix} \tag{10}$$

$$\lambda = \begin{Bmatrix} 0.043 + 17.81a - 39.85a^2 + 36a^3 & for\ \ 0 < a < 1 \\ 14 + 1.4(a - 1) & for\ \ 1 \le a \le 3 \end{Bmatrix} \tag{11}$$

Diffusion flux of the water through the electrolyte is calculated:

$$\Omega_{H_2O} = D_w \cdot A \cdot \frac{\left(\vec{C}_2 - \vec{C}_1\right)}{t_{mea}} \tag{12}$$

where t_{mea} and D_w are the thickness of the electrolyte and the diffusion coefficient of the water transport through the electrolyte, respectively. The water diffusion coefficient through the Nafion® membrane is calculated with consideration of the membrane water content [21]:

$$D_w = D_\lambda \cdot \exp\left[2416 \cdot \gamma \left(\frac{1}{303} - \frac{1}{T}\right)\right] \tag{13}$$

2.2.6. Liquid water transport

The saturation factor should be determined in order to calculate the liquid water transport based on the capillary pressure [22]:

$$s = \frac{(v_{H_2O})_l}{v_{pore}} = \frac{\vec{C}_{H_2O} - \vec{C}_{sat}}{\frac{\rho_l}{M_{H_2O}} - \vec{C}_{sat}} \qquad \vec{C}_{H_2O} > \vec{C}_{sat}$$
$$s = 0 \qquad \vec{C}_{H_2O} \le \vec{C}_{sat} \tag{14}$$

Liquid water transport through GDL is driven by the capillary pressure gradient:

$$P_c = \tau \cos(\theta_c) \left(\frac{\varepsilon}{K}\right)^{\frac{1}{2}} J(s) \tag{15}$$

where P_c, τ, $J(s)$, and K are the capillary pressure, the surface tension, the Leverette function, and the permeability, respectively.

2.2.7. Pressure drop

The head loss is determined by the friction factor, which is calculated based on the Reynolds number [23]:

$$hd = f \frac{L}{D_H} \frac{V^2}{2\vec{g}} \tag{16}$$

2.2.8. Electrochemical model

The net voltage is determined by subtracting the activation and the ohmic overvoltage from the local Nernst voltage:

$$V_{net} = V_{Nernst} - V_{activation} - V_{ohmic} - V_{concentration} \tag{17}$$

The Nernst voltage is calculated based on the concentrations of the reactant gas at the triple phase boundary, and the electrolyte temperature [24]:

$$V_{Nernst} = \left(-\frac{\Delta G(T)}{n \cdot F} + \frac{R \cdot T}{n \cdot F} \ln\left[\frac{a_{H_2} \cdot a_{O_2}^{\frac{1}{2}}}{a_{H_2O}}\right] \right)_{gdl} \tag{18}$$

The activation overvoltage is determined by the Tafel equation based on the electrolyte temperature, the water saturation and the oxygen concentration at cathode GDL 4 in order to capture the effect of liquid water through the GDL on the PEMFC performance [24]:

$$V_{activation} = \frac{RT_{gdl}}{anF} \ln\left(\frac{i}{i_o}\frac{\left(\vec{C}_{O_2}\right)_o}{\vec{C}_{O_2}}\frac{1}{1-s}\right) \quad (19)$$

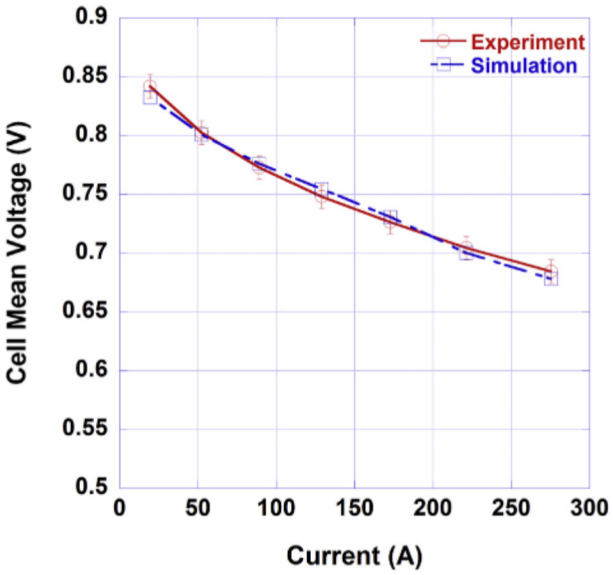

Fig. 3. Comparison of current–voltage polarization curve between the experiment and simulation.

Table 2
The operating conditions for PEMFC stack dynamic validation.

Parameters	Units	Values
Temperature at anode inlet	°C	30
Temperature at cathode inlet	°C	30
Relative humidity at anode inlet	%	20
Relative humidity at cathode inlet	%	20
H_2 utilization factor	–	0.8
Air utilization factor	–	0.5

$$i_o = (i_o)_{ref} \exp\left(-\frac{E_{ref}}{RT}\left(1-\frac{T}{T_{ref}}\right)\right) \quad (20)$$

where, i_o and $(C_{O_2})_o$ are the reference value of the exchange current density and the oxygen concentration, respectively. The ohmic overvoltage is calculated for the Nafion® based on the membrane water content and the electrolyte temperature [25].

$$V_{ohmic} = i\frac{t_{mea}}{(0.005139\lambda - 0.00326)\cdot\beta\cdot\exp\left(1268\left(\frac{1}{303}-\frac{1}{T_{mea}}\right)\right)} \quad (21)$$

2.3. Air blower

The dynamic response of the air blower is relatively slow compared with the electrochemical reaction of the PEMFC stack, which is a crucial factor to determine the system dynamics. To accurately investigate the system dynamic behavior, the lumped air blower dynamic model was developed by modifying our previous model [26]. After the system power controller had determined the load current of the PEMFC stack, the desired air flow rate was calculated as follows [27]:

$$\left(\dot{N}_{air}\right)_{target} = \frac{i \times N_{FC} \times \lambda_{air}}{4 \times F \times \vec{X}_{O_2}} \quad (22)$$

where i, N_{FC}, and λ_{air} are the current, cell number, and air stoichiometric ratio, respectively. F and $\vec{X}_{O_2}$ are the Faraday number and the oxygen mole fraction, respectively. Subsequently, the input voltage was supplied to the air blower to drive the motor. The motor torque of the blower was determined using a static motor equation as follows:

$$\tau_{motor} = \eta_{motor}\frac{\kappa_t}{R_{motor}}(V_{motor} - k_v\omega_{blower}) \quad (23)$$

where η_{motor} is the motor mechanical efficiency and κ_t, R_{motor}, and k_v are the motor constants. The demand torque required to drive the blower was calculated using the following thermodynamic equation [28]:

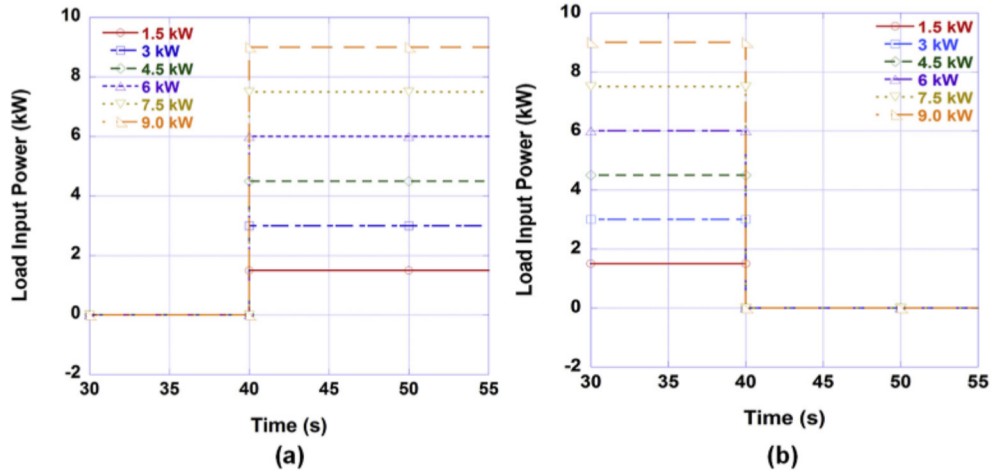

Fig. 4. Changes in step load input power of the PEMFC–battery hybrid system.

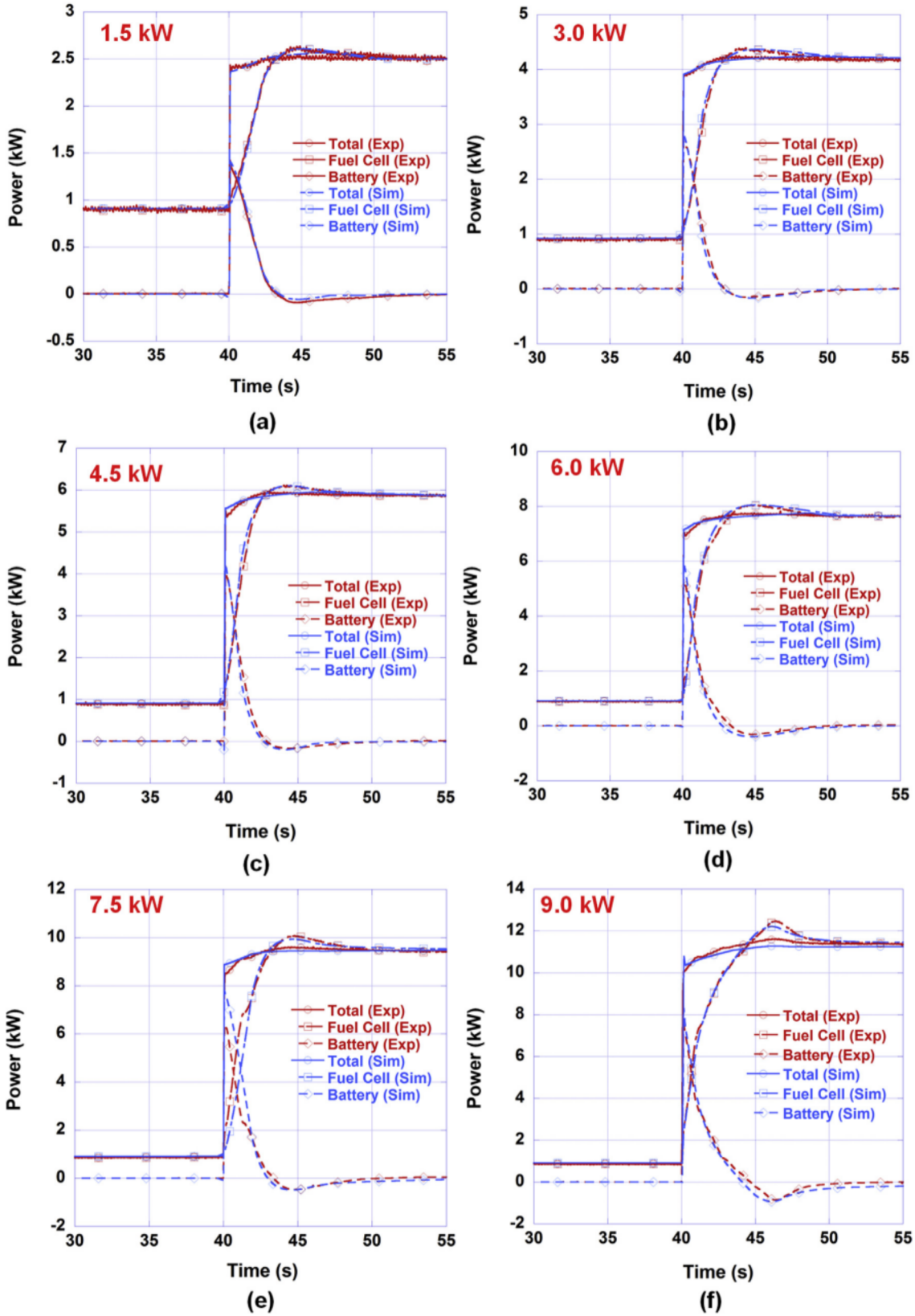

Fig. 5. Comparison of power generated by PEMFC stack and battery between the simulation and experiment at the step load power increase from 0 to 1.5, 3.0, 4.5, 6.0, 7.5, and 9.0 kW.

$$\tau_{blower} = \frac{C_p\left(\dot{N}_{air}\right)_{actual}\Delta T}{\omega_{blower}} \tag{24}$$

where ω_{blower} represents the blower speed. The dynamic response of the blower speed was calculated by considering the motor and blower inertia.

$$J_{blower}\frac{d\omega_{blower}}{dt} = \tau_{motor} - \tau_{blower} \tag{25}$$

where J_{blower} is the total inertia of the motor and the blower. After

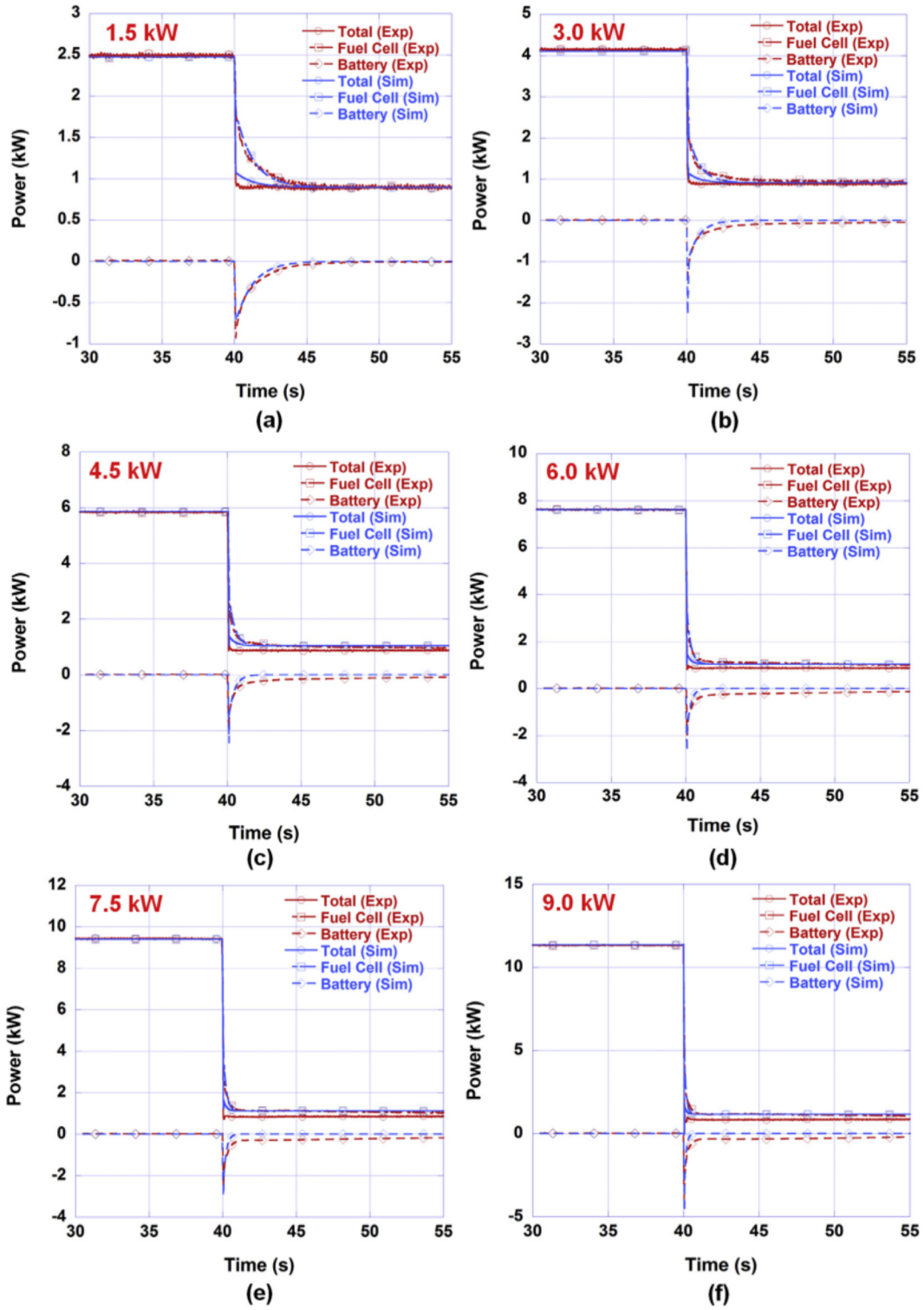

Fig. 6. Comparison of power generated by PEMFC stack and battery between the simulation and experiment at the step load power decrease from 1.5, 3.0, 4.5, 6.0, 7.5, and 9.0 kW to 0.

calculating the blower speed, the air flow rate was determined on the basis of the blower map from the blower speed across the pressure ratio.

2.4. Battery

The lumped dynamic battery model was developed using the RC–ladder model. The dynamic behavior of the battery output voltage at the step change of the load power was determined by considering the short-term response, long-term response, and internal resistance [29].

$$V_b = OCV_b + i_b \cdot (C_{b,s} + C_{b,l} + R_b) \tag{26}$$

where OCV_b, i_b, R_b, $C_{b,s}$, and $C_{b,l}$ are the open-circuit voltage, current, resistance, short-time constant, and long-time constant of battery, respectively.

The initial voltage of the battery was obtained from the map performance data of the SOC-OCV. Further, the SOC was acquired by integrating the battery internal current from the initial value of the SOC.

$$SOC = SOC_{initial} + \int_0^t i_b \tag{27}$$

3. Experimental setup

To evaluate the steady- and dynamic-state performance of the in-rack PEMFC–battery hybrid system, the Hydrogenics HyPM™ 10 kW Rack (a PEMFC system with a maximum power of 12 kW) connected to the APC Smart-UPS™ VT™ 15 kVA UPS system (with lead-acid batteries) has been installed and used for the experiment [1]. The air and hydrogen flow rates were controlled by the blower and valves, respectively. To maintain the PEMFC stack temperature, the coolant water was circulated through the cooling channel of the PEMFC stack. Further, the coolant water could be cooled down by tap water via a heat exchanger [1]. The exhaust gas from the anode and cathode of the PEMFC stack was removed by the ventilation blower [1].

The Yokogawa® WT1600 digital power meter was used to measure the power from the PEMFC and the battery with a sample

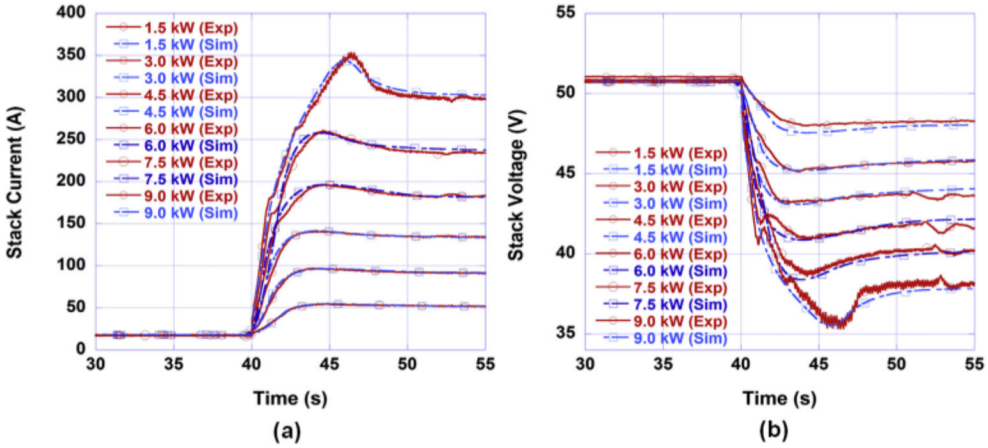

Fig. 7. Comparison of PEMFC stack current and voltage between the simulation and experiment at the step load power increase from 0 to 1.5, 3.0, 4.5, 6.0, 7.5, and 9.0 kW.

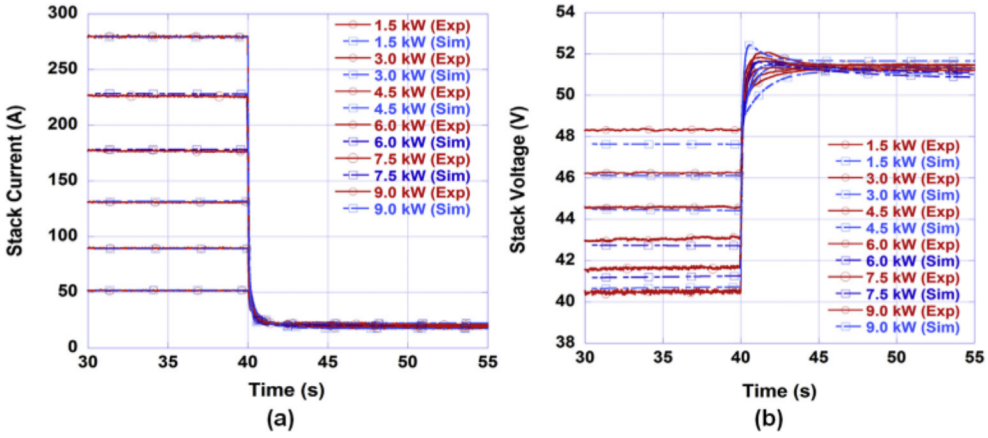

Fig. 8. Comparison of PEMFC stack current and voltage between the simulation and experiment at the step load power decrease from 1.5, 3.0, 4.5, 6.0, 7.5, and 9.0 kW to 0.

time of 50 ms. The Alicat® hydrogen flow meter (M-250SOPM-D/CM) was utilized to measure the hydrogen flow rate with 500 ms resolution. The air flow rate, anode pressure, and coolant temperature were acquired with a sampling time of 10 s. Three Chroma® 63803 programmable AC electronic load banks were used to control the magnitude of the AC load applied to the hybrid system. The type of server used in the experiment was a 750-W HP® Proliant SE326M1 with two quad-core CPUs and 98 GB memory.

4. Simulation results and discussion

4.1. Model verification at steady state

To verify the PEMFC stack model at steady state, the current–voltage polarization curve from the model was compared with the experimental data, as shown in Fig. 3. Table 2 presents the operating conditions. As mentioned previously, both the hydrogen and air were not heated and humidified before entering the stack. In this validation, the inlet temperature and inlet humidity of hydrogen and air was set to 30 °C and 20%, respectively. The utilization factor of hydrogen and air was 0.8 and 0.5, respectively. The simulation data are in good agreement with the experimental data with a minimal error of ±0.01 V over the entire current density region.

4.2. Model validation during transients

The dynamic behavior of the PEMFC–battery hybrid system model was compared with the experimental data at the step change of the external load power. The external load power was instantly increased or decreased between the loads of 0 and 1.5, 3.0, 4.5, 6.0, 7.5, and 9.0 kW at 40 s, as shown in Fig. 4. As mentioned previously, when the PEMFC–battery hybrid system is activated, the ventilation blower begins to operate, and it consumes 0.71 kW regardless of the magnitude of the external load power [1]. Figs. 5 and 6 present the comparison of the total, stack, and battery power between the experiment and simulation at an instant increase and decrease of the external load power. Although the error between the model and experiment increased with the rising load power, the simulation data is well matched with the experimental data with minimal error in every case. When the PEMFC–battery hybrid system was operated as the step load increases, the system instantly obtained the total amount of external load power from the battery due to the fast response of the battery. Subsequently, the fuel cell gradually supplied power to the system. That is, the discharging rate of the current from the battery is immediately increased from 40 s to 40.1 s in every case and gradually decreased until approximately 44 s or 46 s as the power generated by the fuel cell is gradually increased. Hence, the overshoot behavior appeared in the stack power variation because of the undershoot behavior of the stack voltage variation and the variation in the power consumed by the air blower. The magnitude of the overshoot behavior increased with the increase in the external load power. Meanwhile, when the external load is instantly decreased to zero, the charge rate of the current from the battery is immediately increased up to 30.05 s and subsequently gradually decreased as the fuel cell power continuously decreases.

As mentioned previously, when a certain magnitude of the

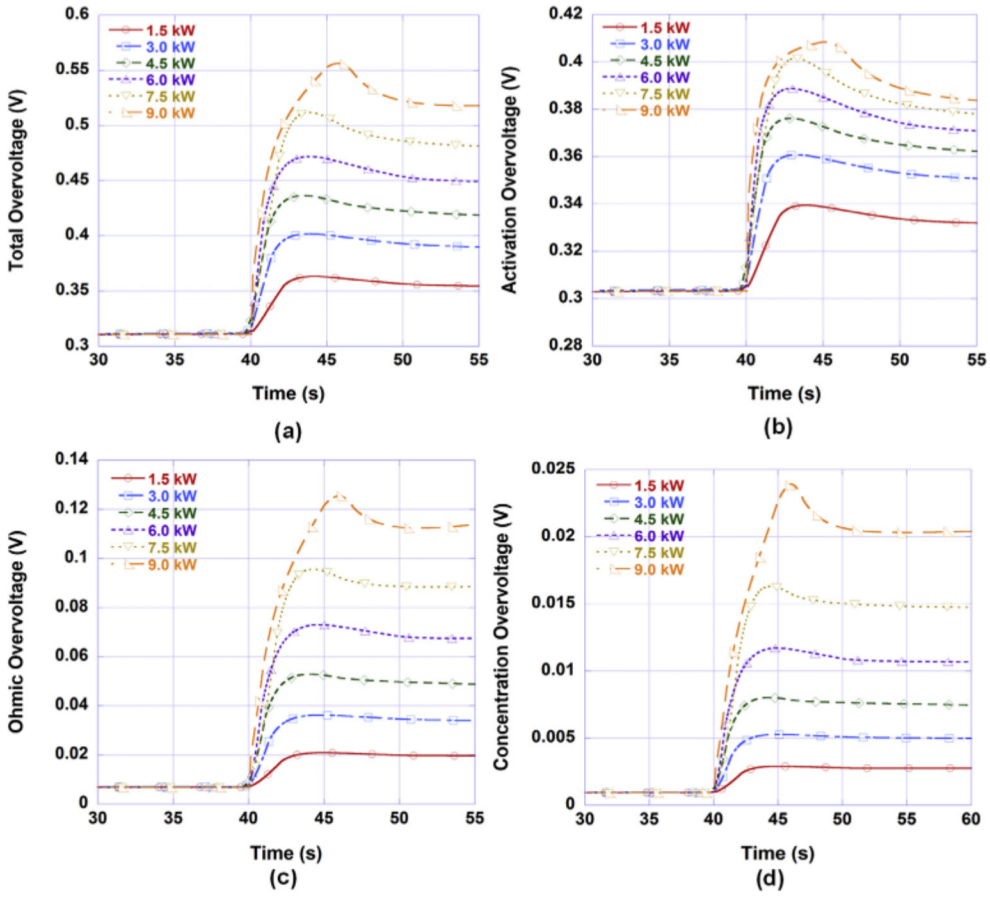

Fig. 9. Variations in activation, ohmic, and concentration overvoltages at the step load power increase from 0 to 1.5, 3.0, 4.5, 6.0, 7.5, and 9.0 kW.

external load power is demanded to the stack, the system power controller instantly determines the stack input current. Figs. 7 and 8 show the variation in the stack current and stack voltage at the step increase or decrease of the external load, respectively. When the external load is increased, the input stack current is gradually increments from 40 s to 46 s. Further, the undershoot behavior appears in the voltage variation. In addition, the magnitude of the voltage undershoot increases with the increment in the external load power. Because the stack power was obtained by multiplying the stack current and stack voltage, the overshoot behavior in the stack current variation is due to the expected behavior in the voltage variation. Similarly, when the external load is suddenly decreased to zero, the input stack current was rapidly decreased also, but the stack output voltage was immediately increased. Although the overshoot behavior of the voltage variation appeared, the undershoot behavior in the stack current did not appear due to the small magnitude of voltage overshoot. These undershoot and overshoot behaviors of the stack voltage were caused by the time difference among the variation in the stack input current, reactant concentration at the reaction sites, and water hydration through the electrolyte. That is, when the stack input current is rapidly increased or decreased, the required value of both the reactant concentration at the reaction sites and water content through the electrolyte should be quickly increased or decreased. However, the reactant concentration at the reaction sites is not instantly increased or decreased due to mass transport resistance in the channel and GDL, the time constants for the species diffusion through GDL is milliseconds [30]. The water content through the electrolyte were determined by the water flux through the electrolyte such as electro-osmotic drag and water diffusion. The time scale of the water accumulation through the electrolyte is tens of seconds [30]. Water accumulation is more critical factor to determine the dynamic behavior of the PEMFC than species diffusion through the GDL due to its larger time scale. The overshoot or undershoot behavior of the activation and concentration overvoltage was caused by the time duration for the mass transport of the reactant concentration. Further, the time duration for the membrane hydration results in the overshoot or undershoot behavior in the ohmic overvoltage variation.

Figs. 9 and 10 present the variations in activation, ohmic, concentration, and total overvoltage during external load changes. The overvoltage and undershoot behaviors separately appeared in their variations. The magnitude of the undershoot was relatively small compared with that of the overshoot. Fig. 11-(a) and 12-(a) show the variations in the power consumed by the air blower at the increase and decrease of the external load power, respectively. Because the activation overvoltage at the cathode was much higher than that at the anode, the dynamic behavior of the air blower was crucial to determine the dynamic behavior of the overall system. In addition, the target air flow rate was determined on the basis of the magnitude of the input current. Further, the inertia of the motor and blower caused the time delay of the air flow rate variation, thus affecting the oxygen concentration variation at the cathode, resulting in the dynamic behavior of the activation overvoltage. Fig. 11-(b) and 12-(b) show the variations of the battery SOC at the increase and decrease of the external load power, respectively. The SOC of the battery was gradually decreased up to approximately 43 s and continuously increased, and it subsequently reached another state with increase of the external load. With the decrease in external load, the battery SOC was gradually increased. The

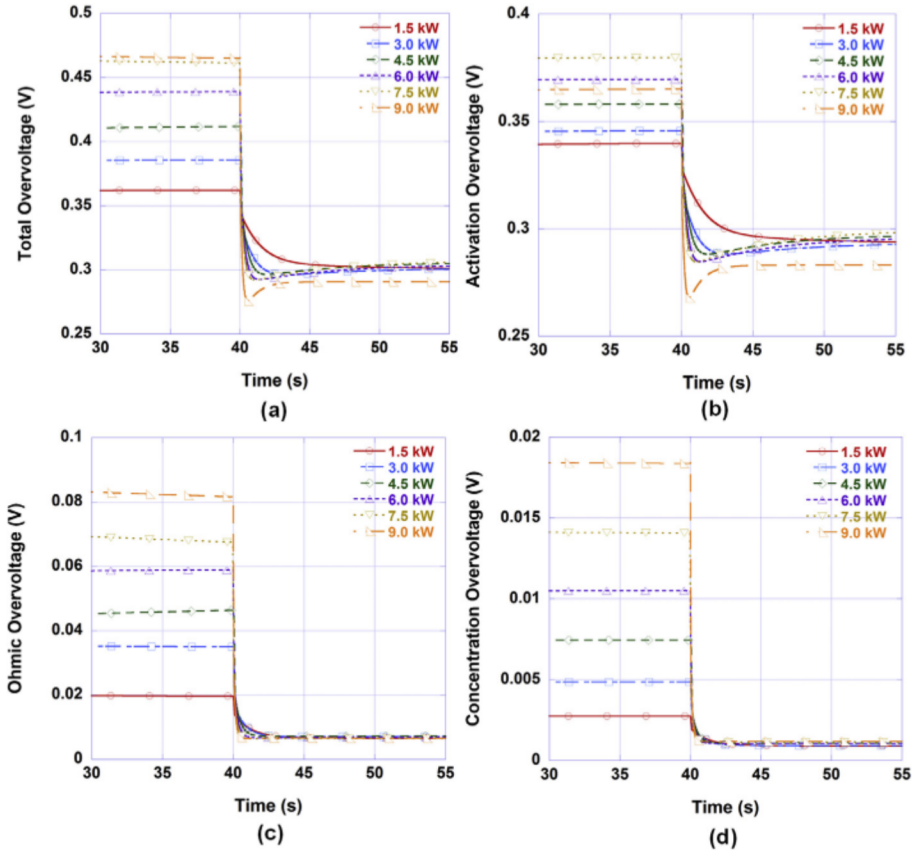

Fig. 10. Variations in activation, ohmic, and concentration overvoltages at the step load power decrease from 1.5, 3.0, 4.5, 6.0, 7.5, and 9.0 kW to 0.

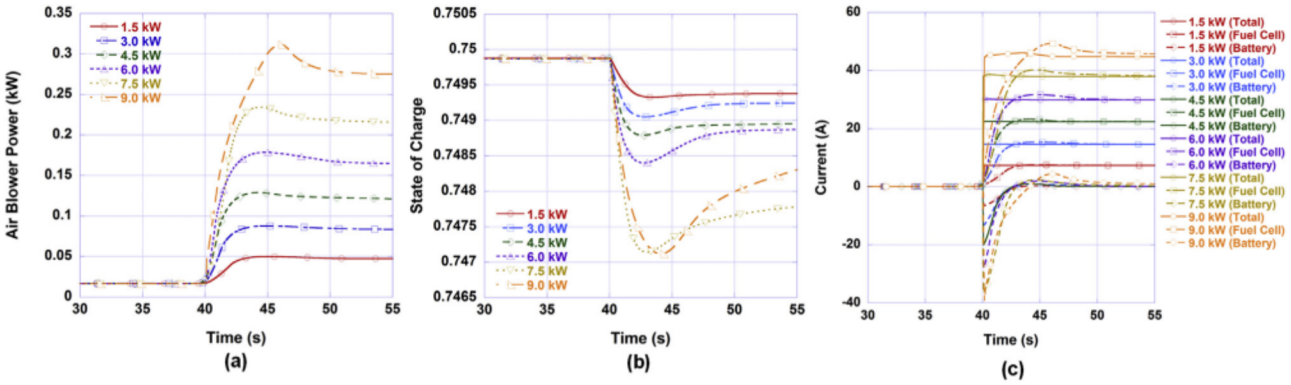

Fig. 11. Variations in power consumed by air blower, battery SOC, and current of PEMFC stack and battery from 0 to 1.5, 3.0, 4.5, 6.0, 7.5, and 9.0 kW.

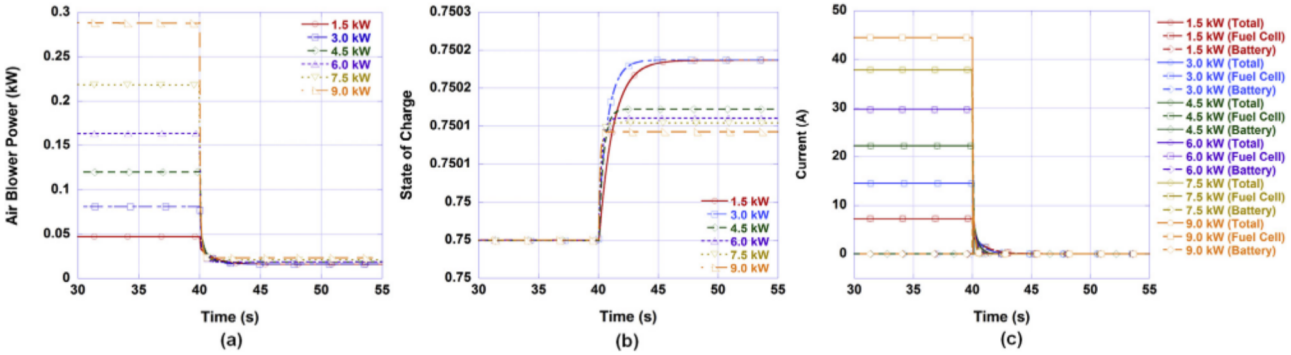

Fig. 12. Variations in power consumed by air blower, battery SOC, and current of PEMFC stack and battery from 1.5, 3.0, 4.5, 6.0, 7.5, and 9.0 kW to 0.

variation in the battery SOC was determined by the battery current variation. Fig. 11-(c) and 12-(c) present the current variation from the stack and battery at the increase and decrease of the external load power, respectively. When the dynamic behavior of the battery is higher than that of the fuel cell stack, the battery is immediately discharged or charged by the total amount of current and subsequently gradually charged or discharged by the current supplied from the stack.

To investigate the dynamic characteristics of the system with various server loads, the system model was also simulated with the external load of three, six, and nine servers, respectively. Fig. 13 presents the comparison of the power variations of the fuel cell and battery between the experiment and simulation. The right figure is a close-up of the left one to verify the difference between the model and simulation at the most perturbed period of the server load. The simulation results of the stack and the battery power variation were in good agreement with those of the experiment. At the first spike of the power variation, the battery instantly supplied the total amount of power and the fuel cell started to ramp up the power, and it subsequently supplied a high portion of power from the second spike. Fig. 14 shows the activation, ohmic, and concentration overvoltage variations under various server loads, all of which exhibited a similar tendency to the stack power variation. Fig. 15 shows the variation in the current supplied from the fuel cell and battery during various server load changes. The battery instantly discharged the total amount of demand current at the first spike, and it subsequently decreased the discharge rate as the current supplied from the stack was increased. Meanwhile, the amount of current generated by the stack was increased; subsequently, a high portion of current was supplied from the second spike. Fig. 16-(a) presents the variations in the battery SOC. The battery SOC is gradually decreased from 30 s to 39 s and maintained with slight fluctuation. Fig. 16-(b) shows the water flux through the cathode GDL in the PEMFC. The positive sign indicates the water flux toward the cathode GDL. At an instant load power change, the water generation by the electrochemical reaction and the water flux by the electro-osmotic drag suddenly changed. Subsequently, the diffusion through the GDL and electrolyte gradually changes. In this simulation, the capillary water flux did not appear because of the low value of the inlet humidity and input current. The variations in the water flux affected the water content value through the electrolyte, which determines the ohmic overvoltage variation, and finally the performance of the PEMFC system.

5. Conclusions

The dynamic model of the PEMFC–battery hybrid system was developed using the MATLAB–Simulink® software and verified by comparing its performance at steady and dynamic states with the experimental data. The PEMFC–battery hybrid system consisted of a one-dimensional, two-phase dynamic model of the PEMFC stack, lumped dynamic model of an air blower, lumped dynamic battery model, and system power controller. The PEMFC was discretized into 11 and 15 control volumes in the perpendicular flow direction to resolve the mass and energy conservation, respectively. The PEMFC model considered the two-phase water transport through the GDL to investigate the liquid water effect on the performance. The zero-dimensional dynamic model of the air blower was developed by considering the inertia of the motor and blower. The lumped dynamic battery model was developed using the R–C ladder model. Furthermore, the system power controller based on the PI controller was developed to determine the input current

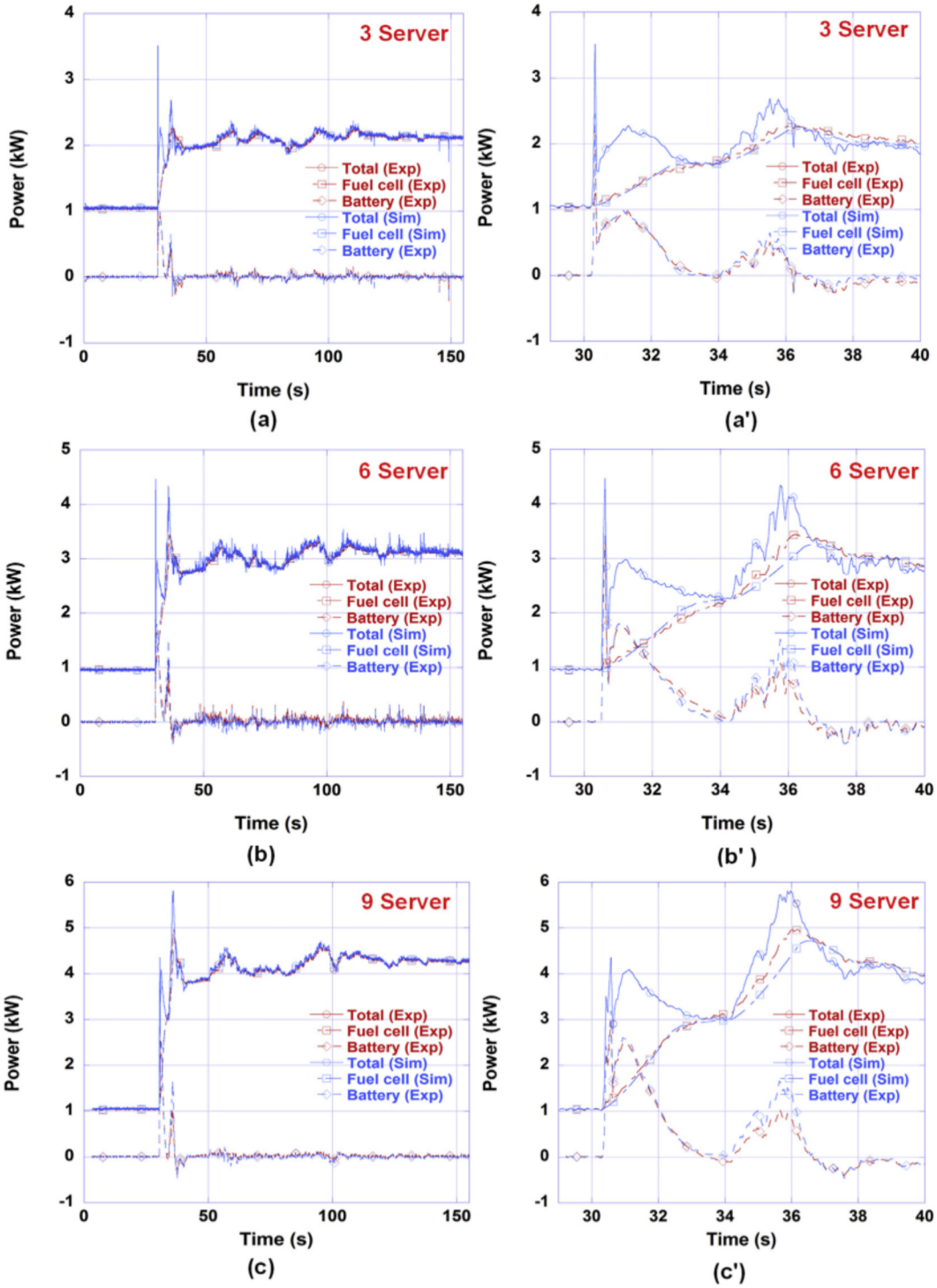

Fig. 13. Comparison of power generated by PEMFC stack and battery between modeling results and experimental data at various load changes of three, six, and nine servers.

with varying input load power.

The PEMFC–battery hybrid system model was validated by comparing the dynamic behavior of the respective power generation of the PEMFC stack and battery with the experimental data at the step change of the external load power between 0 and 1.5, 3.0, 4.5, 6.0, 7.5, and 9.0 kW. The dynamic performance of the system model was also compared with the experimental data with the demand load profiles of three, six, and nine servers. The model well predicts the experimental data with minimal error. The variations in the PEMFC characteristics of water flux and irreversible voltage loss and the BOP characteristics of the battery SOC and the power consumed by the air blower were also determined at various load and server load changes.

The proposed model is beneficial in determining the dynamic behavior of the PEMFC–battery hybrid system under various load changes at different operating conditions. Hence, the model is expected to contribute in establishing an optimal control strategy of the PEMFC–battery hybrid system to power servers in data centers.

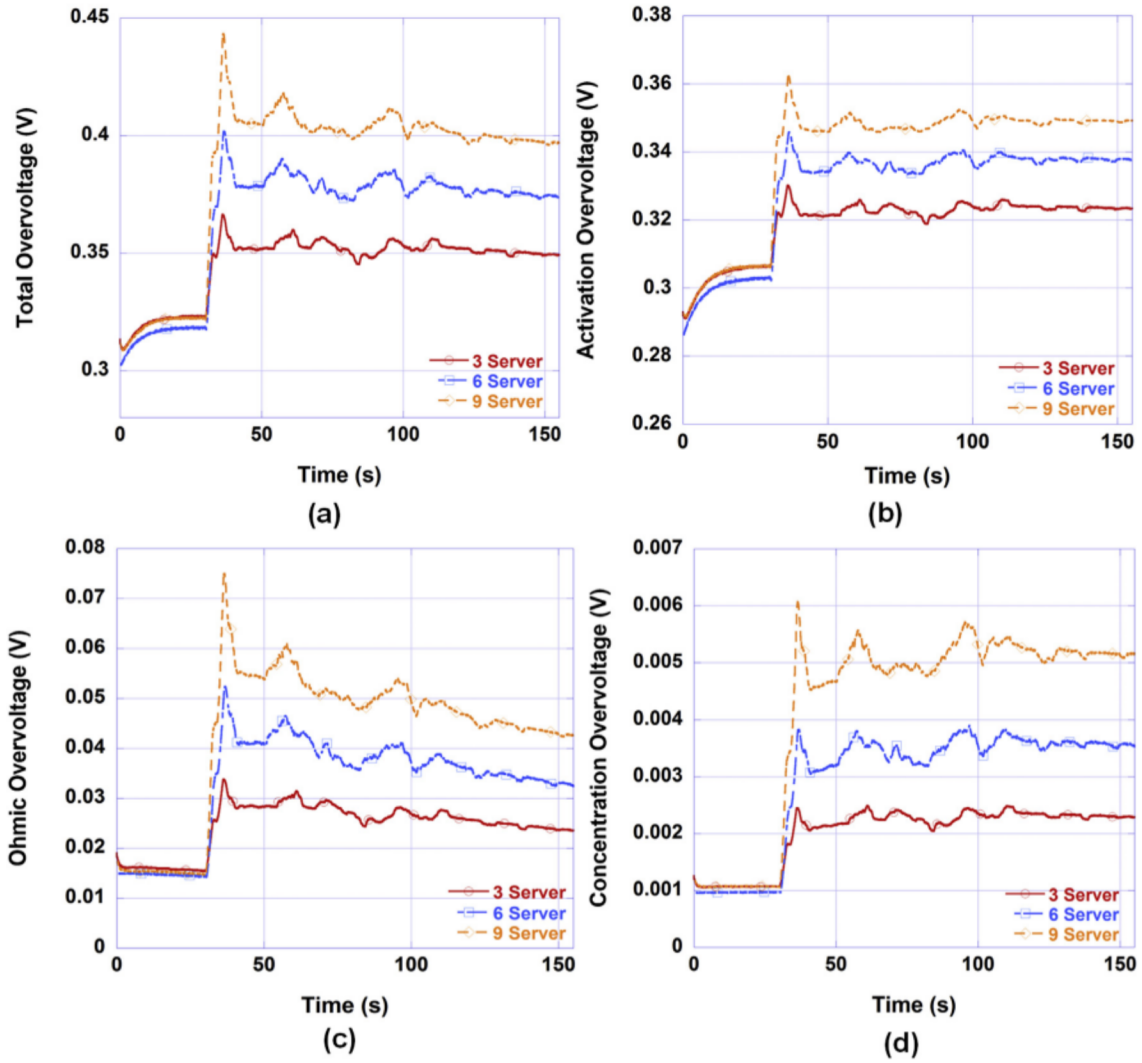

Fig. 14. Activation, ohmic, and concentration overvoltage variations at various load changes of three, six, and nine servers.

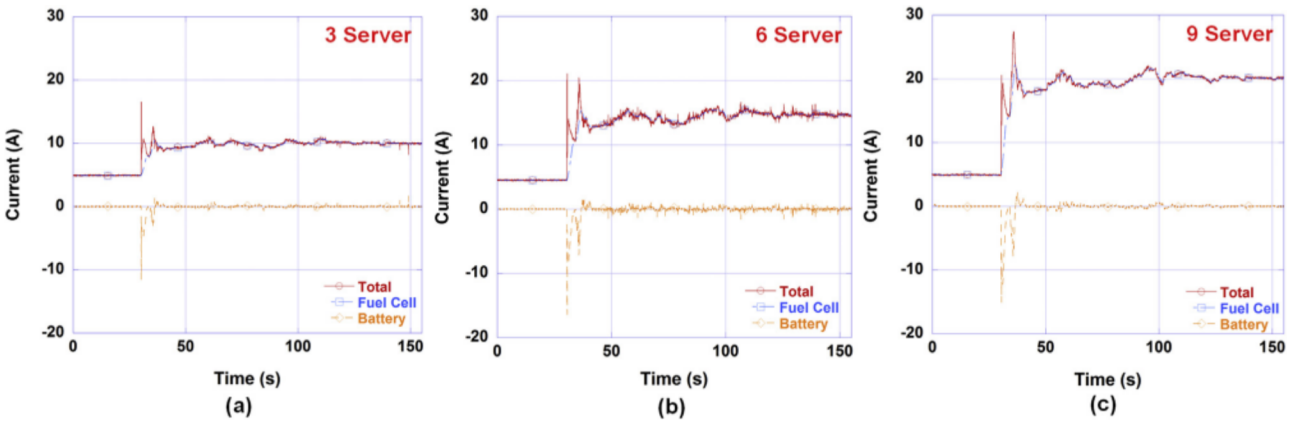

Fig. 15. Variations in currents of PEMFC stack and battery at various load changes of three, six, and nine servers.

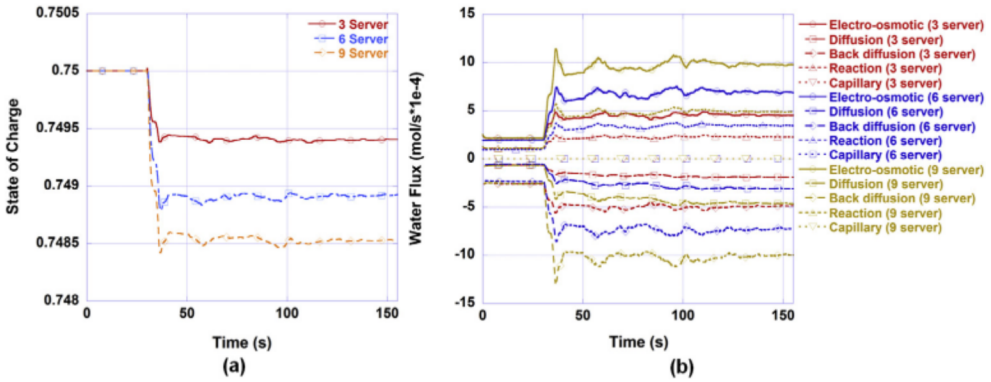

Fig. 16. Variations in battery SOC and water flux through the GDL in PEMFC stack at various load changes of three, six, and nine servers.

Acknowledgments

This work was supported by the Technology Development Program to Solve Climate Changes of the National Research Foundation (NRF) grant funded by Korean Government (Ministry of Science and ICT) (NRF-2017M1A2A2045196).

References

[1] L. Zhao, J. Brouwer, S. James, J. Siegler, E. Peterson, A. Kansal, J. Liu, Dynamic performance of an in-rack proton exchange membrane fuel cell battery system to power servers, Int. J. Hydrogen Energy 42 (2017) 10158–10174.
[2] L. James, A. Dicks, Fuel Cell Systems Explained, Jonn Wiley & Sons Ltd, 2009.
[3] Y. Wang, K.S. Chen, J. Mishler, S.C. Cho, X.C. Adroher, A review of polymer electrolyte membrane fuel cells: Technology, applications, and need on fundamental research, Appl. Energy 88 (2011) 981–1007.
[4] A. Shehabi, S. Smith, D. Sartor, R. Brown, M. Herrlin, J. Koomey, E. Masanet, N. Horner, I. Azevedo, W. Lintner, United states Data Center Energy Usage Report, 2016.
[5] Sverdlik Y. eBay's Utah Data Center Offers a Glimpse into the Future N.d.
[6] Y. Tang, W. Yuan, M. Pan, Z. Li, G. Chen, Y. Li, Experimental investigation of dynamic performance and transient responses of a kW-class PEM fuel cell stack under various load changes, Appl. Energy 87 (2010) 1410–1417.
[7] K.H. Loo, K.H. Wong, S.C. Tan, Y.M. Lai, C.K. Tse, Characterization of the dynamic response of proton exchange membrane fuel cells – a numerical study, Int. J. Hydrogen Energy 35 (2010) 11861–11877.
[8] J. Cho, T. Ha, J. Park, H.-S. Kim, K. Min, E. Lee, J.-Y. Jyoung, Analysis of transient response of a unit proton-exchange membrane fuel cell with a degraded gas diffusion layer, Int. J. Hydrogen Energy 36 (10) (2011) 6090–6098.
[9] F. Tiss, R. Chouikh, A. Guizani, Dynamic modeling of a PEM fuel cell with temperature effects, Int. J. Hydrogen Energy 38 (2013) 8532–8541.
[10] A. Gomez, A. Raj, A.P. Sasmito, T. Shamim, Effect of operating parameters on the transient performance of a polymer electrolyte membrane fuel cell stack with a dead-end anode, Appl. Energy 130 (2014) 692–701.
[11] B. Kim, D. Cha, Y. Kim, The effects of air stoichiometry and air excess ratio on the transient response of a PEMFC under load change conditions, Appl. Energy 138 (2015) 143–149.
[12] Y. Tang, W. Yuan, M. Pan, Z. Wan, Experimental investigation on the dynamic performance of a hybrid PEM fuel cell/battery system for lightweight electric vehicle application, Appl. Energy 88 (2011) 68–76.
[13] L. Barelli, G. Bidini, A. Ottaviano, Optimization of a PEMFC/battery pack power system for a bus application, Appl. Energy 97 (2012) 777–784.
[14] K. Ettihir, L. Boulon, K. Agbossou, Optimization-based energy management strategy for a fuel cell/battery hybrid power system, Appl. Energy 163 (2016) 142–153.
[15] F. Peng, Y. Zhao, X. Li, Z. Liu, W. Chen, Y. Liu, D. Zhou, Development of master-slave energy management strategy based on fuzzy logic hysteresis state machine and differential power processing compensation for a PEMFC-LIB-SC hybrid tramway, Appl. Energy 206 (2017) 346–363.
[16] Z. Hong, Q. Li, Y. Han, W. Shang, Y. Zhu, W. Chen, An energy management strategy based on dynamic power factor for fuel cell/battery hybrid locomotive, Int. J. Hydrogen Energy 43 (2018) 3261–3272.
[17] H. Li, A. Ravey, A. N'Diaye, A. Djerdir, A novel equivalent consumption minimization strategy for hybrid electric vehicle powered by fuel cell, battery and supercapacitor, J. Power Sources 395 (2018) 262–270.
[18] H. Fathabadi, Combining a proton exchange membrane fuel cell (PEMFC) stack with a Li-ion battery to supply the power needs of a hybrid electric vehicle, Renew. Energy 130 (2019) 714–724.
[19] S. Kang, K. Min, Dynamic simulation of a fuel cell hybrid vehicle during the federal test procedure-7 driving cycle, Appl. Energy 161 (2016) 181–196.
[20] T.A. Zawondzinski, J. Davey, J. Valerio, S. Gottesfeld, The water contents dependence of electro-osmotic drag in proton-conducting polymer electrolytes, Electrochim. Acta 40 (1994) 297–302.
[21] S. Motupally, A.J. Becker, J.W. Weidner, Diffusion of water in Nafion 115 membranes, J. Electrochem. Soc. 147 (2000) 3171–3177.
[22] Y. Wang, Modeling of two-phase transport in the diffusion media of polymer electrolyte fuel cells, J. Power Sources 185 (2008) 261–271.
[23] F.M. White, Fluid Mechanics, sixth ed., Mcgrawhill, 2008.
[24] J. Tafel, Uber die polarization bei kathodischer wasserstoffentwicklung, Zeitschrift fur Physikalische Chemie 50 (1905) 641–712.
[25] T.E. Springer, T.A. Zawodzinski, S. Gottesfeld, Polymer electrolyte fuel cell model, J. Electrochem. Soc. 138 (1991) 2334–2341.
[26] S. Kang, K. Min, S. Yu, Dynamic modeling of a proton exchange membrane fuel cell system with a shell-and-tube gas-to-gas membrane humidifier, Int. J. Hydrogen Energy 37 (2012) 5866–5875.
[27] R. O'Hayre, S.W. Cha, W. Colella, F.B. Prinz, Fuel Cell Fundamentals, second ed., John Wiley & Sons, 2009.
[28] M.P. Boyce, Gas Turbine Engineering Handbook, Gulf Publishing, 1982.
[29] Kang S, Kim H, Chae S, Song Y. European PEFC and H2 Forum 2013.
[30] Brouwer J. Mueller, S. Kang, H.-S. Kim, K. Min, Quasi-three dimensional dynamic model of proton exchange membrane fuel cell for system and controls development, J. Power Sources 163 (2007) 814–829.